Journal of Solid State Chemistry 184 (2011) 3280–3288

Contents lists available at SciVerse ScienceDirect

Journal of Solid State Chemistry

journal homepage: www.elsevier.com/locate/jssc

Correlation of optical properties and temperature-induced irreversible phase transitions in europium-doped yttrium carbonate nanoparticles

Ray Gunawidjaja, Thandar Myint, Hergen Eilers *

Applied Sciences Laboratory, Institute for Shock Physics, Washington State University, Spokane, WA 99210-1495, USA

ARTICLE INFO

Article history:
Received 3 June 2011
Received in revised form
16 August 2011
Accepted 9 October 2011
Available online 15 October 2011

Keywords:
Thermometry
Europium-doped yttria
Nanoparticles
Structural changes
Optical properties

ABSTRACT

Nanophase europium-doped yttrium carbonate precursors are subjected to heat treatments, ranging from 300 °C to 1100 °C for dwell times of 5 min, 30 min, and 180 min. XRD, TEM, FT-IR, fluorescence, fluorescence excitation, and fluorescence lifetime measurements are used to characterize the materials. Upon heating, the material transitions through several amorphous stages until it reaches the crystalline cubic Y_2O_3 phase. DSC measurements show an exothermic transition at 665.7 °C, indicating the formation of crystalline Y_2O_3. The grain size development is fitted by the relaxation equation and yields an activation energy of 50.3 kJ/mol. The amorphous phases are characterized by inhomogenously broadened optical spectra. Heating up to 700 °C leads to an increased fluorescence lifetime (from about 1 ms to 2.4 ms). As the material is heated to higher temperatures and completes the formation of the crystalline cubic Y_2O_3 phase, the optical spectra become narrower and the fluorescence lifetime decreases to about 1.2 ms.

1. Introduction

Europium-doped inorganics are of interest for thermometric applications [1,2]. In these applications, the fluorescence lifetime or the fluorescence intensity is measured and compared to calibration data to determine the temperature. In general, this technique requires line of sight or fiber-optics to monitor the optical signal. However, some situations, e.g. explosions are either too hazardous and/or conceal the optical signature and thus no in-situ measurements can be performed. In such situations it is necessary to find ex-situ forensic measurement techniques.

In explosions that are used to destroy biological or chemical agents, nanoparticles are of interest because these particles can travel with the simulant agent and sense and record the local temperature profile. In addition, the high surface-to-volume ratio of nanoparticles allows for a uniform heat distribution within the particles. Ex-situ applications require that the material is capable of recording and storing the thermal history so that it can be read-out and analyzed at a later time. Such recording and storing of information can be accomplished if the material undergoes irreversible temperature-induced structural changes that can be measured after the actual event has passed. Rare-earth ions such as Eu^{3+} can be used to monitor such structural changes via their optical characteristics.

Loosely agglomerated nanosized europium-doped yttrium oxide (Y_2O_3:Eu) of uniform dimensions can be prepared by means of combustion synthesis [3], aerosol synthesis [4], sol–gel synthesis [5], and homogeneous precipitation [6] from its salt precursors at mild or moderate heating conditions. In some cases, materials prepared in this manner, require subsequent heat-treatment to fully transform the salt precursors to oxides. During the heat-treatment, which typically exceeds 500 °C for the formation of the crystalline Y_2O_3 phase, the nanoparticles undergo a gradual and irreversible change in their chemical composition and their crystalline quality, and thereby alter the optical characteristics of the material [7–9]. We report here on the morphological and optical properties of europium doped yttrium carbonate nanopowders that undergo thermal treatment via furnace heating (300–1100 °C for dwell times between 5 min and 180 min). In addition, grain size analysis is performed on samples heated for dwell times up to 48 h.

2. Materials and methods

Y_2O_3:Eu (1 mol% Eu) precursors are prepared via a coprecipitation method by adding, under continuous stirring, an aqueous mixture of ammonium hydroxide and ammonium bicarbonate (1:1 mol ratio, 1.25 M) dropwise to a europium nitrate ($Eu(NO_3)_3 \cdot 5H_2O$, 99.999%)/yttrium nitrate ($Y(NO)_3 \cdot 6H_2O$, 99.999%) solution (1:99 mol ratio) [10]. The pH of the solution is monitored to reach a final value of 7.5–8.0. After 3 h of aging at room temperature (under continuous stirring), the white precipitates are washed with DI-water (3 ×) and acetone (1 ×). The precipitates are dried in vacuum overnight to

* Corresponding author. Fax: +1 509 358 7627.
E-mail address: eilers@wsu.edu (H. Eilers).

0022-4596/$ - see front matter © 2011 Elsevier Inc. All rights reserved.
doi:10.1016/j.jssc.2011.10.013

remove acetone and then at 150 °C for 12 h to remove water. Finally, the dried white cake is crushed into powder with mortar and pestle.

The dried nanopowders are heat-treated in a Lindberg Blue box-furnace using a heating rate of 25 °C per minute. After the furnace reached the set temperature of 300 °C, 500 °C, 700 °C, 900 °C, or 1100 °C, the samples were left at these temperatures for dwell times ranging from 5 min to 48 h. The furnace was then allowed to cool down at its natural cooling rate. Optical characterization was performed on the samples heated for dwell times between 5 min and 3 h. Grain size analysis was performed for samples of all dwell times.

Transmission electron microscopy (TEM) images are obtained using a Philips CM 200. Differential scanning calorimetry (DSC) and thermogravimetric analysis (TGA) measurements are performed using a Netzch STA 409 PCat with a ramp rate of 20 °C/min between 30 °C and 1200 °C under Ar atmosphere. X-ray diffraction (XRD) spectra are obtained with a PANalytical X'PERT Pro Diffractometer using Cu$K\alpha$ radiation. The grain sizes are estimated using the Rietveld method from the X-ray diffraction patterns with the aid of X'pert Highscore Plus software [11]. Fourier transform infrared spectra are acquired with a Varian (Agilent) 680-FT-IR spectrometer.

Excitation and fluorescence spectra, as well as fluorescence lifetimes of the samples are measured using a Continuum Power-Lite 8000 Nd:YAG laser in combination with a Continuum Panther optical parametric oscillator (OPO) and an Acton 2750 monochromator with a photomultiplier tube (PMT) (see Fig. 1). The Nd:YAG laser is operating at 10 Hz and emits third-harmonic pulses (355 nm) of 5–7 ns duration. This output is used to pump the OPO, which emits pulses of 3–7 ns duration with a linewidth of less than 5 cm^{-1}. Using several mirrors, the OPO output is guided to the powder samples. The powder samples are placed in a glass vial and the laser enters from top. Emission is observed in a 90° configuration. A 50.8 mm diameter lens with a focal length of 15 cm is used to collect the fluorescence, while a 50.8 mm lens with a focal length of 50 cm is used to focus the emission on the entrance slit of the Acton 2750 monochromator with an f number of 9.7. A Hamamatsu R955 photomultiplier is used to detect the fluorescence. An Acton SpectraHub connected to a computer with WinSpec/SpectraSense software is used to control the monochromator and collect the data. The slit width of the monochromator is set to 750 μm for the excitation measurements and 250 μm for the fluorescence measurements, resulting in a bandpass of about 1.5 nm for excitation measurements and 0.5 nm for fluorescence measurements. Because signal intensities vary over a wide range for the different samples, absorbing neutral density filter are used in front of the monochromator slits when needed.

3. Results and discussion

3.1. Characteristics of the co-precipitated yttria precursor

The use of mixed precipitants, ammonium hydroxide and ammonium bicarbonate, leads to the formation of nanosized morphologies (see Fig. 2(a)). Since the nanoparticles tend to aggregate, it is not possible to accurately measure the particle size. The particles have irregular shapes with dimensions in the 20–50 nm range. Nanoparticles prepared in this manner are known to favor the formation of de-agglomerable (soft agglomerate) oxide powders upon calcination [12]. X-ray diffraction measurements show that the as-prepared precipitate is amorphous, as seen from the broad halo curve in Fig. 2(b). It is worth noting that at a pH greater than 9.0, the nanosized particles are known to form two-dimensional microstructures. However, this formation was avoided in this work by keeping the pH at a lower value. According to Huang et al. [10], at a lower pH the precipitate consists of $Y_2(CO_3)_3 \cdot nH_2O$, while at higher pH the $Y_2(CO_3)_3 \cdot nH_2O$ species transform into $Y(OH)CO_3$. The hydroxyl group in $Y(OH)CO_3$ is capable of forming oxo-bridges that lead to the formation of micron-sized aggregates. As they spontaneously assemble into micro-aggregates, the yttrium hydroxide nanoparticles tend to assemble more rapidly in the direction perpendicular to the resulting plane of two-dimensional micro-structures. Upon calcination, $Y(OH)CO_3$ powders form hard agglomerate [10].

Fig. 2(c) shows the FT-IR spectrum of the amorphous precursor. The absorption peaks at 1520 cm^{-1} and 1385 cm^{-1} are due to the asymmetric stretching of C–O, and the absorption peaks at 1084 cm^{-1} and 845 cm^{-1} are due to the symmetric and deformation vibration of C–O, respectively, indicating the presence of carbonate ions. The band between 800 cm^{-1} and 650 cm^{-1} is due to the deformation vibration of CO_3^{2-} [13]. The broad absorption peak at 3440 cm^{-1} is due to the H–O–H stretching mode of lattice water. The accompanying H–O–H deformation vibration band at about 1645 cm^{-1} is not apparent and may be masked by the peak at 1520 cm^{-1} that extends to about 1800 cm^{-1} [14]. The 1645 cm^{-1} peak does become more pronounced as a shoulder in some of the heated samples (see for example Fig. 4(d)). As the heating temperature increases, the contribution of CO_3^{2-} to the spectra is diminished due to release of CO_2 (compare relative contributions of the 3440 cm^{-1} and 1520 cm^{-1} peaks). While the absence of a narrow structural O–H peak at about 3528 cm^{-1} would imply that the precursor is $Y_2(CO_3)_3$ [15,16], this peak may be masked by the larger 3440 cm^{-1} peak and thus the presence of $Y(OH)CO_3$ cannot be ruled out.

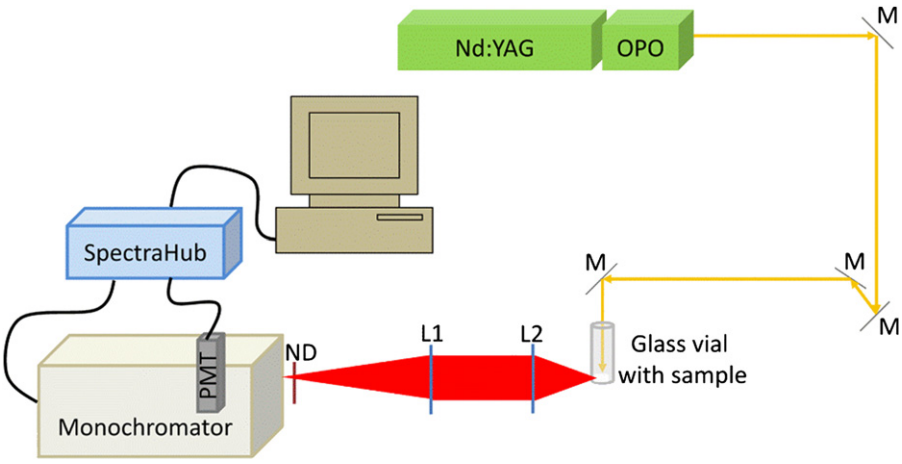

Fig. 1. Experimental setup for excitation, fluorescence, and fluorescence lifetime measurements.

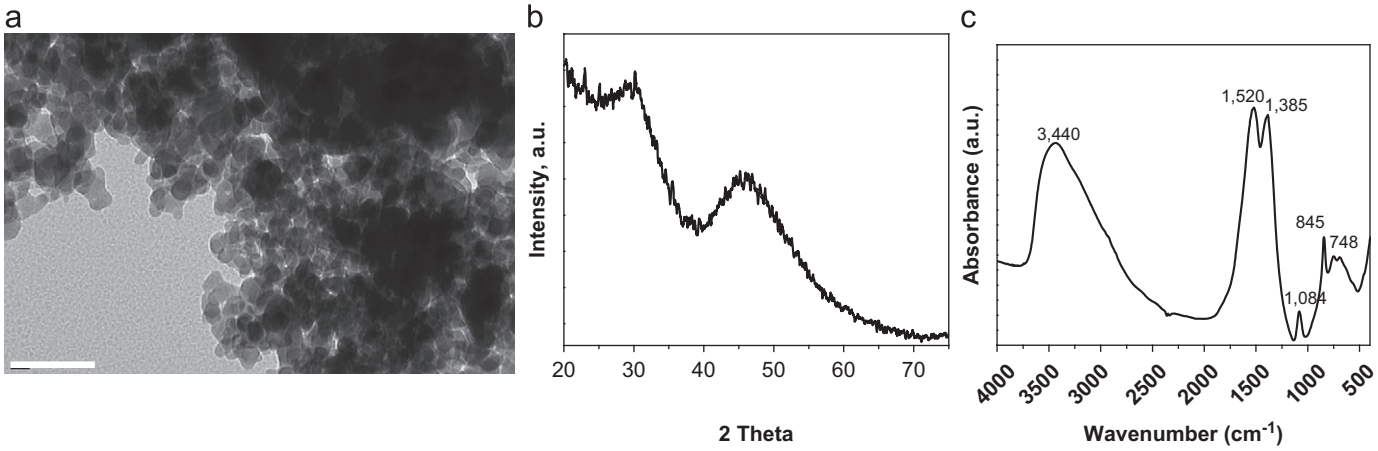

Fig. 2. (a) TEM image (scale bar is 100 nm), (b) XRD spectrum, and (c) FT-IR spectrum of co-precipitated yttria precursor.

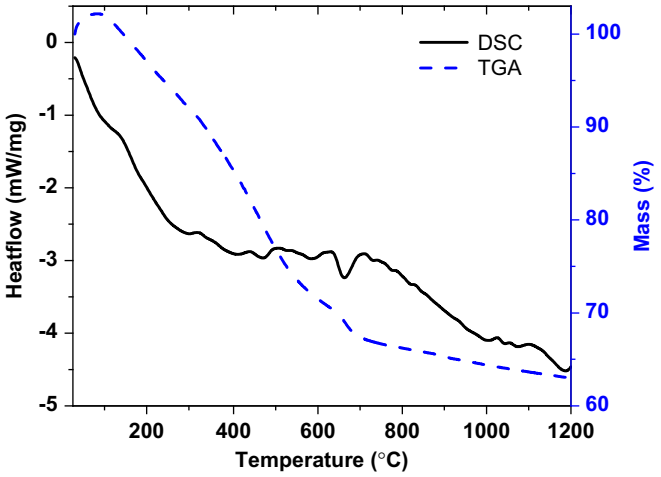

Fig. 3. DSC and TGA curves of the co-precipitated yttria precursor.

3.2. Characteristics of the heat-treated yttria precursor

Between room temperature and 700 °C, the TGA curve shows a continuous mass loss of up to about 33 wt% (see Fig. 3). This large mass loss is consistent with the yttria precursor being either $Y_2(CO_3)_3$ or $Y(OH)CO_3$ or a mixture of them [17]. The DSC curve shows an exothermic transition at 665.7 °C. This transition is due to the formation of Y_2O_3 following the decomposition [18]. Above this temperature, the rate of mass loss is significantly reduced, indicating an almost completed formation of the Y_2O_3 phase. Due to prior drying (see Section 2), no apparent endothermic transitions in the 100–150 °C range, corresponding to loss of water, were observed. The overall decomposition steps for yttrium carbonate precursors have been reported previously [10]. The decomposition begins with the loss of water, physisorbed, chemisorbed, and lattice water, followed by the release of CO_2 resulting in $Y_2O(CO_3)_2$. Due to further release of CO_2, $Y_2O(CO_3)_2$ decomposes into $Y_2O_2CO_3$, which finally transforms into Y_2O_3 under loss of CO_2. As such, the expected decomposition processes (under release of CO_2) is

$$Y_2(CO_3)_3 \rightarrow Y_2O(CO_3)_2 \rightarrow Y_2O_2CO_3 \rightarrow Y_2O_3 \quad (1)$$

If $Y(OH)CO_3$ is present, it will decompose according to

$$Y(OH)CO_3 \rightarrow Y_2O_2CO_3 \rightarrow Y_2O_3 \quad (2)$$

The last step in both the reactions is the same and leads to the formation of yttrium oxide.

The initial formation of Y_2O_3 is corroborated by the appearance of an FT-IR absorption peak at 570 cm^{-1}, which is indicative of Y–O bonds (see Fig. 4(a)–(e)). The earliest appearances of the Y–O bond can be seen for heating to 500 °C for 5 min (see Fig. 4(b)). The continuous loss of water and decomposition towards the formation of Y_2O_3 is apparent by the relative increase in intensity of the Y–O peak at 570 cm^{-1} compared to the O–H and C–O peaks. However, some remnants of the peaks corresponding to C–O and O–H bonds are still visible even after furnace heating to 1100 °C for 180 min. These peaks are due to surface hydroxyl and carbonate groups that form when Y_2O_3 reacts with ambient water and carbon dioxide, respectively [19].

Fig. 5 shows XRD spectra of yttria precursors heat-treated at various temperatures and dwell times. Fig. 5(a) shows that at 300 °C the matrix remains amorphous even for dwell times of 180 min. The influence of dwell time on the crystal quality is best demonstrated in Fig. 5(b). As the dwell time increases to about 500 °C, the peaks become narrower, indicating the formation of crystalline cubic Y_2O_3. The three highest intensity x-ray diffraction peaks, matching the crystalline cubic Y_2O_3 phase (PDF no. 01-072-0927) at $2\theta = 29.1°$, 48.5°, and 57.6°, start to appear for the sample heated to 500 °C for 30 min. The presence of the cubic crystalline phase of Y_2O_3 is apparent in the spectra of samples heated to 700 °C and above (see Fig. 5(c)–(e)). Since $Y_2O_2CO_3$ is thermally stable only up to 470 °C, the crystalline peaks seen for heating to 500 °C for 30 min are likely to correspond to Y_2O_3 [20]. After a dwell time of 180 min the peaks can be unambiguously matched to the cubic Y_2O_3 phase.

Fig. 6 shows the TEM images of the heated samples. The images show that the samples heated to 500 °C have a perforated appearance, which may be attributed to the carbonate decomposition resulting in the release of carbon dioxide. This decomposition results in smaller particle sizes for samples heated to 700 °C for dwell times of 5 min, 30 min, and 180 min. As will be discussed later, this decomposition process and the resulting lower filling factor of sample material per unit volume affect the radiative lifetime of the material. Above 700 °C, these crystalline particles grow in size with increasing temperature—up to 70–80 nm in diameter for heating to 1100 °C for 180 min. The particle size of this sample, as determined from the TEM image is comparable to the grain size determined from the XRD spectrum, indicating complete crystallization. These particles have polyhedral geometry and are loosely agglomerated.

Fig. 7(a) shows the grain size (determined from XRD data) vs. dwell time for various heating temperatures. The trend in the

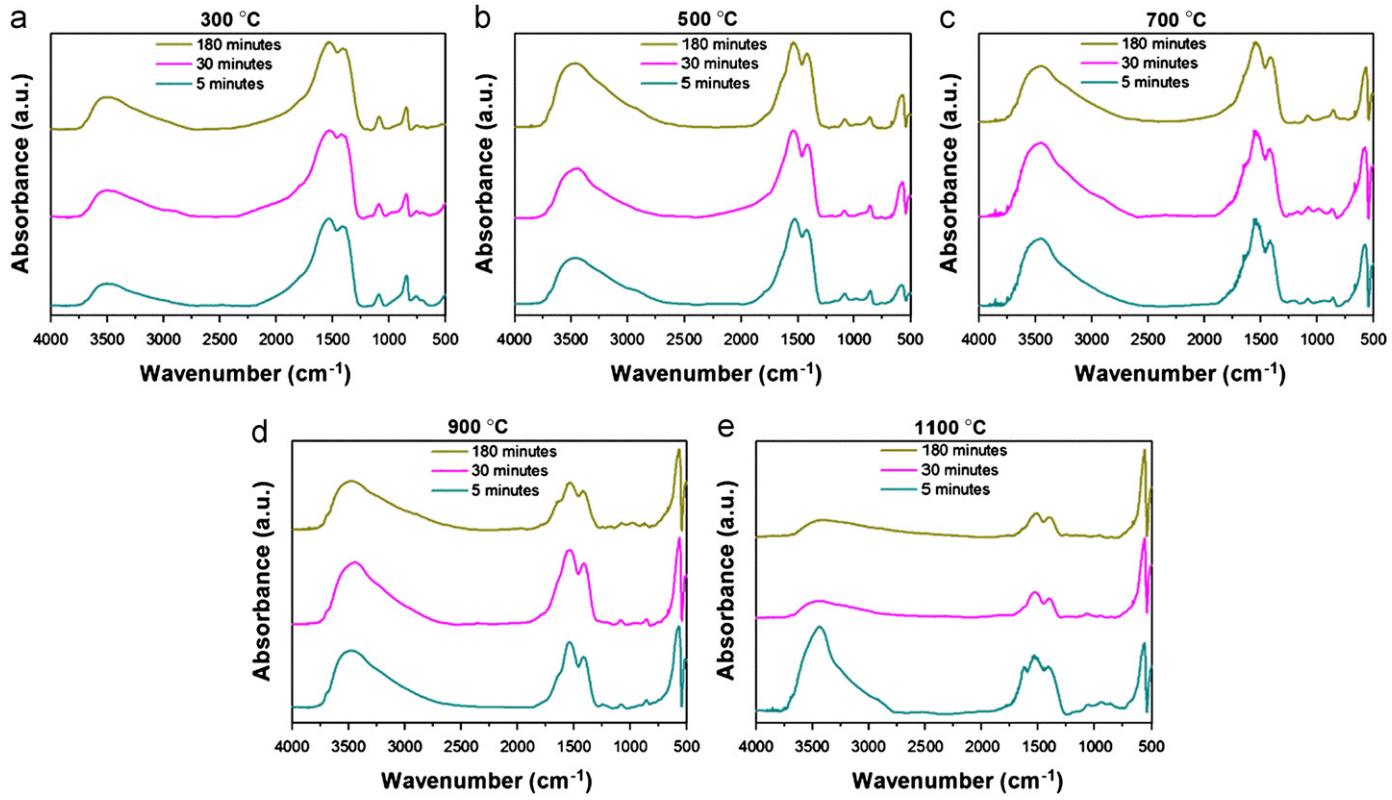

Fig. 4. FT-IR spectra of co-precipitated yttria precursors heat-treated at 300 °C, 500 °C, 700 °C, 900 °C, and 1100 °C for dwell times of 5 min, 30 min, and 180 min.

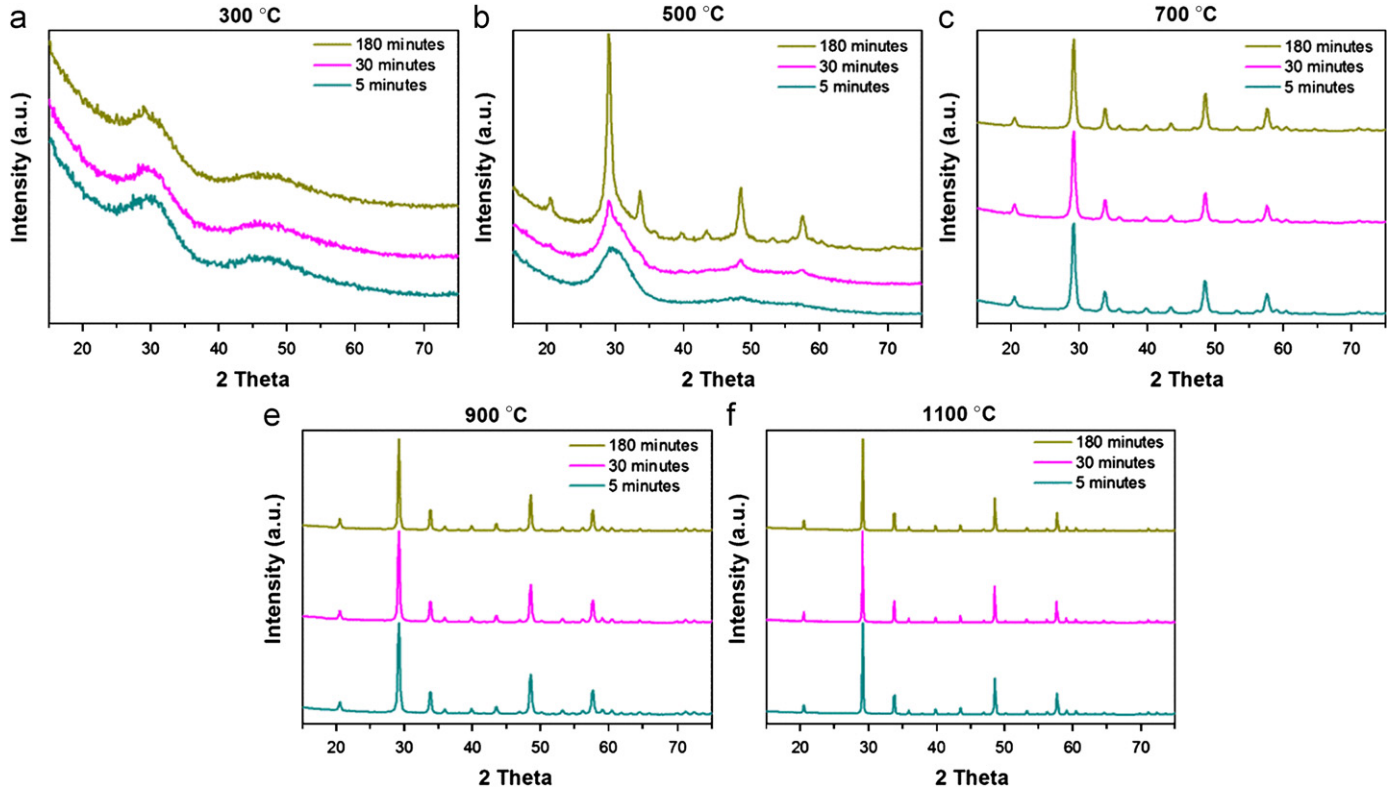

Fig. 5. XRD patterns of co-precipitated yttria precursors heat-treated at 300 °C, 500 °C, 700 °C, 900 °C, and 1100 °C for dwell times of 5 min, 30 min, and 180 min.

crystalline growth is characteristic for nanosized particles [21]. Initially, the grains grow rapidly within a short period of annealing time. This period is followed by a period of substantially slower growth rate, and finally a period in which the growth levels off. During the last stage, the grain size approaches its limiting grain size for a given temperature. No crystalline domain

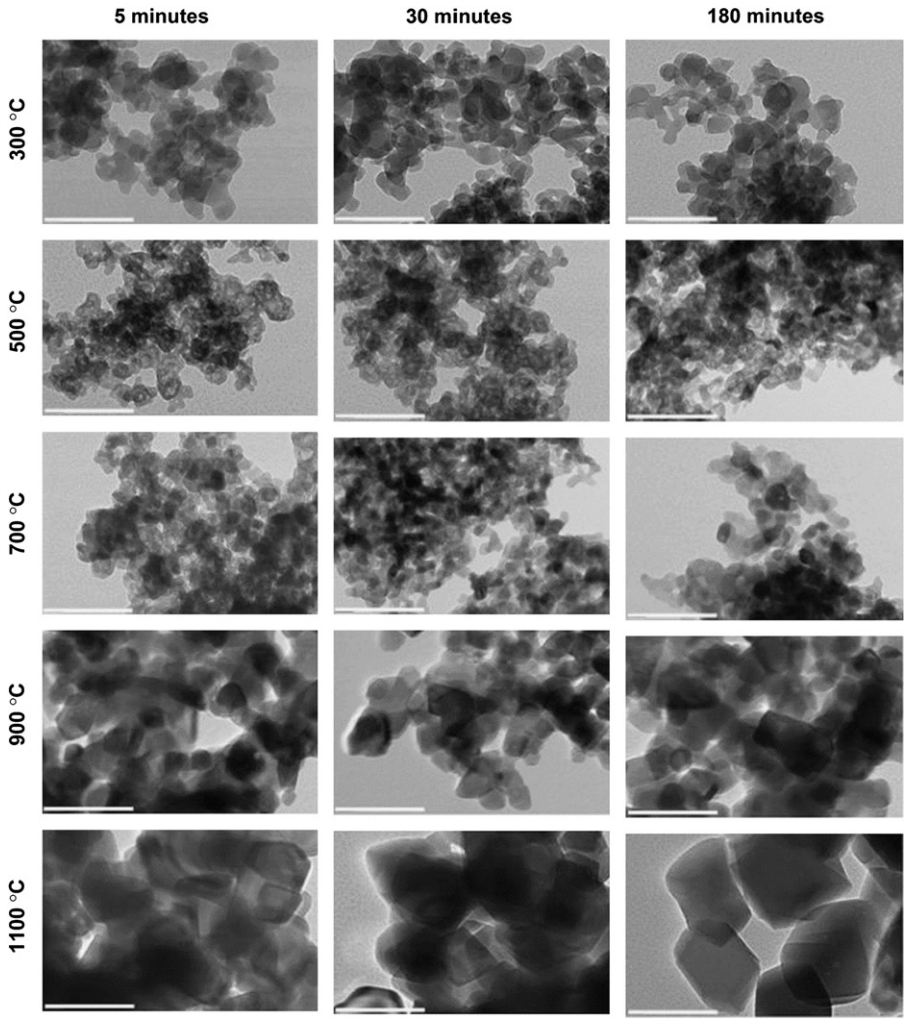

Fig. 6. TEM images of co-precipitated yttria precursor, heat-treated at various temperatures and dwell times. Scale bar is 100 nm.

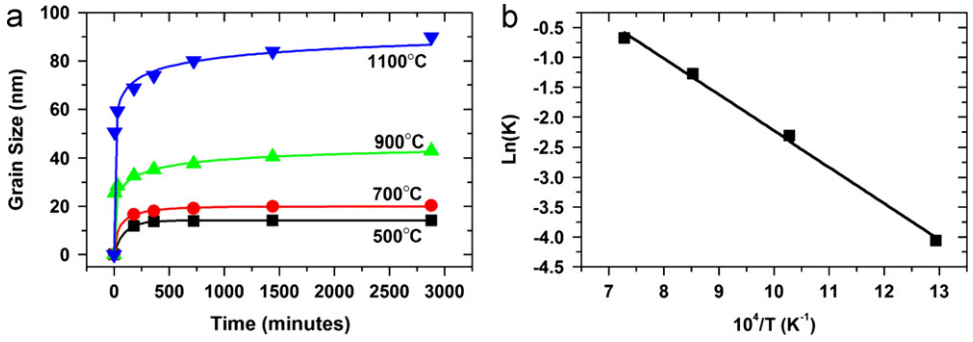

Fig. 7. (a) Grain size vs. dwell time for yttria precursor, heat-treated at various temperatures and dwell times. (b) Plot of Ln(K) vs. $1/T$ (K^{-1}).

is observed at 300 °C. At all higher temperatures, the grain growth slows down considerably after about 2 h.

Fitting of the above data using the conventional grain growth equation [21]:

$$D^n - D_0^n = Kt \tag{3}$$

with D being the average grain size after annealing, D_0 being the initial grain size, n being the grain growth exponent, t being the annealing time, and K being a constant proportional to $\exp(-Q/RT)$ with Q being the activation energy, R being the gas constant, and T being the calcination temperature, yielded different values for the grain growth exponent n for the various calcinations temperatures.

Fitting our data to a structural relaxation equation yielded more consistent results [21]. While all data points for the 900 and 1100 °C isothermals could be fitted to this equation, for the 500 and 700 °C isothermals the data points for dwell times of 5 min and 30 min could not be fitted and were left out. It may be that a different process occurs for the shorter dwell times at lower temperatures.

The relaxation equation

$$\frac{D - D_0}{D_m - D_0} = 1 - e^{-Kt^m} \tag{4}$$

with D_m being the limiting grain size, m being the relaxation order ($=1$ for linear relaxation), and the remaining variables as defined before, describes crystalline growth due to gradual ordering of the bond lengths and bond angles at the nanoparticles' interface [21]. This model has been successfully used to describe isothermal growth of sol–gel synthesized nanoparticles. Fig. 7(b) shows the plot of the log of the rate constant vs. inverse temperature. Fitting of this data set provides the activation energy for the grain growth process. Table 1 shows the fitted parameters for each temperature, as well as the X^2 (chi-square) goodness-of-fit. The fitted activation energy of 50.3kJ/mol is on par with values reported in the literature for nanosized particles [21].

3.3. Optical properties

Eu^{3+} dopants can be used to monitor the structural properties of their host and to gain information about how these properties change in response to stimuli [22]. For example, if the europium ion is located in a site with inversion symmetry, electric dipole transitions are forbidden [23,24]. As the site symmetry is lowered, electric dipole transitions become allowed and the optical spectra change from being dominated by magnetic dipole transitions to being dominated by electric dipole transitions. Also, when the host is amorphous, a variety of sites are available for the europium ions, leading to inhomogeneous broadening of the optical spectra. As the material changes from an amorphous phase to a crystalline phase, the spectra become narrower, indicating the more homogeneous nature of the host material.

Table 1
Fitting parameters for relaxation equation.

Temperature (°C)	K	D_m	m	X^2
500	0.017	14.1	0.90	0.009
700	0.099	20.0	0.55	0.075
900	0.280	46.0	0.28	0.033
1100	0.509	98.0	0.18	4.32

Fig. 8 shows the excitation spectra of europium-doped nanoparticles, monitored at 611 nm and heated to various temperatures (300 °C, 500 °C, 700 °C, 900 °C, and 1100 °C) for dwell times of 5 min, 30 min, and 180 min. Since the fluorescence intensity for the different samples varies greatly, neutral density filters of up to OD=2 are used to attenuate the emission from the samples heated to high temperatures to reduce them to a level comparable with that of the sample heated to 300 °C. The excitation spectra of the samples heated to 300 °C for all dwell times show a broad peak centered at about 578.3 nm. As the temperature increases, this broad peak decreases rapidly and instead, a sharp peak centered at about 580.8 nm ($^7F_0 \rightarrow {}^5D_0$) and some weak double peaks at about 568 nm and 570 nm appear. The broad excitation peak centered at about 578.5 nm disappears with increasing temperature. This disappearance is due to the decomposition of the amorphous yttrium carbonate phase. As seen in Fig. 8, the full-width-half-max (FWHM) of the narrow peak at 580.8 nm, representing the formation of the crystalline Y_2O_3 phase, continues to decrease with increasing temperature [25]. No obvious distinctions are apparent in the excitation spectra of samples heated for different dwell times.

Tissue and Yuan observed similar excitation spectra for Y_2O_3:Eu synthesized via gas-phase condensation [26]. Their samples contained only amorphous and crystalline Y_2O_3:Eu, but no carbonates. While theirs and our crystalline peaks are located at almost the same wavelength, the peak of the amorphous phase (annealed at 300 °C) is located at about 579.5 nm for the sample analyzed by Tissue and Yuan and at about 578.5 nm for the sample analyzed by us. In addition, there is less overlap between the amorphous and the crystalline excitation peaks in our spectra compared to the spectra shown by Tissue and Yuan. This difference may be due to the expected presence of amorphous carbonate-containing phases and less amorphous oxide. The data would indicate that the amorphous carbonate phases are excited at shorter wavelength than the amorphous oxide phase.

Fig. 9 shows the peak widths of the excitation spectra as a function of temperature for three dwell times. The width was determined by fitting a Gram–Charlier peak function to the excitation spectra. The peak width decreases with increasing

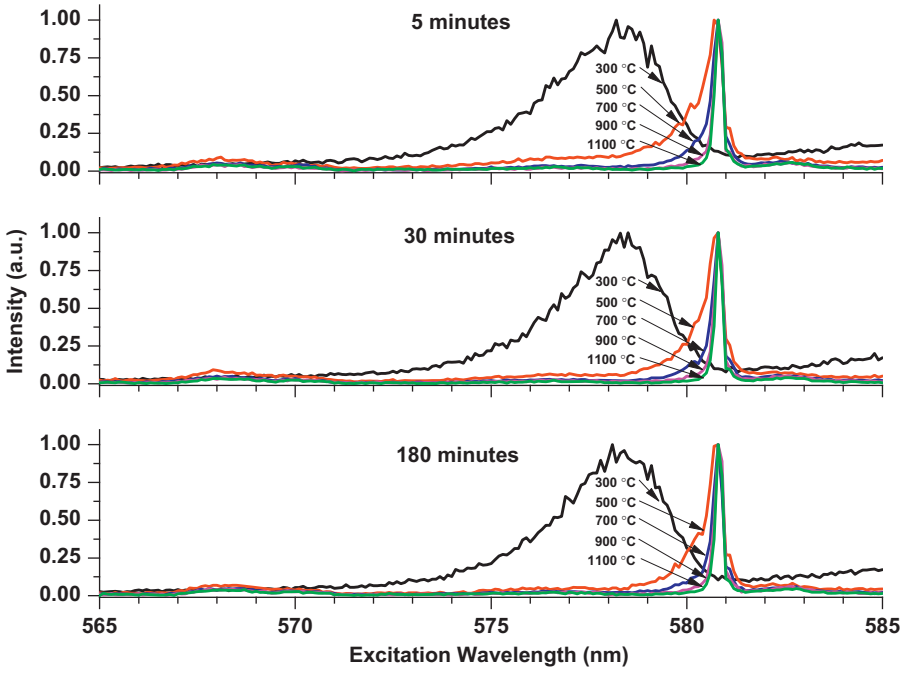

Fig. 8. Normalized excitation spectra of Eu-doped yttria precursor calcined at various temperatures for 5 min (top), 30 min (middle), and 180 min (bottom), observed at 611 nm.

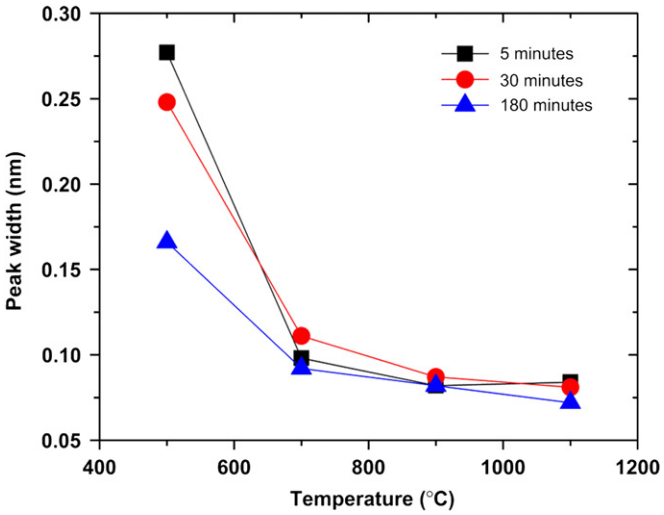

Fig. 9. Peak width of excitation spectra (see Fig. 8) vs. temperature for 5 min, 30 min, and 180 min dwell times.

temperature for all dwell times. For temperatures of 700 °C and above, the dwell time has very little effect on the peak width and temperature appears to be the main driver for the decrease in peak width. As shown in the DSC curve (Fig. 3), for temperatures of 700 °C and above, the material is expected to be in the crystalline Y_2O_3:Eu phase. Once this phase has formed, temperature is the main driver for the reduction of the peak width. On the other hand, grain growth (as shown in Fig. 7) shows a significant dependence on time for dwell times as long as about 250 min.

The fluorescence spectra of the samples heated to 300 °C, 500 °C, 700 °C, 900 °C, and 1100 °C for dwell times of 5 min, 30 min, and 180 min are shown in Fig. 10. Unlike the rest of the samples, the samples heated to 300 °C were excited at 577 nm, in the broad excitation peak for the amorphous phase (excitation at 580.8 nm does not result in an observable signal). As such, they cannot be directly compared with the remaining spectra and are shown only for informational purpose. Excitation of the samples heated to 300 °C at 577 nm resulted in broad emission lines centered at about 620 nm. The samples heated to 500 °C, 700 °C, 900 °C, and 1100 °C were excited at 580.8 nm, leading to emission centered at about 611 nm, typical for crystalline Y_2O_3:Eu. The peaks between 585 nm and 605 nm are due to the $^5D_0 \rightarrow {}^7F_1$ transition, the peaks between 610 nm and 635 nm are due to the $^5D_0 \rightarrow {}^7F_2$ transition, and the peaks around 650 nm are due to the $^5D_0 \rightarrow {}^7F_3$ transition [27]. While the FWHM of the excitation peak of the crystalline Y_2O_3 phase continues to decrease with temperature, the FWHM of the $^5D_0 \rightarrow {}^7F_2$ fluorescence of the crystalline Y_2O_3 phase does not show any apparent decrease. This difference can be understood in terms of energy transfer from Eu^{3+} in the amorphous phase (larger splitting between $^7F_0$ and $^5D_0$) to Eu^{3+} in the crystalline phase (smaller splitting between $^7F_0$ and $^5D_0$). Eu^{3+} to Eu^{3+} energy transfer at low concentrations has been observed by Debasu et al. [28]. Similar to the excitation spectra, no obvious distinctions are apparent in the fluorescence spectra of samples heated for different dwell times.

Fig. 11(a) shows the fluorescence lifetime traces of samples heated for 180 min to various temperatures. All traces were fitted with a single exponential decay, resulting in low X^2 (chi-square) values between 0.0004 and 0.0013. Fig. 11(b) shows a summary of the fluorescence lifetimes of the various europium-doped samples. The data for the three samples (5 min, 30 min, and 180 min) are very close to each other. Samples heated to low temperatures start out at about 1–1.2 ms. As the temperature of the samples is increased, the fluorescence lifetime increases and reaches a

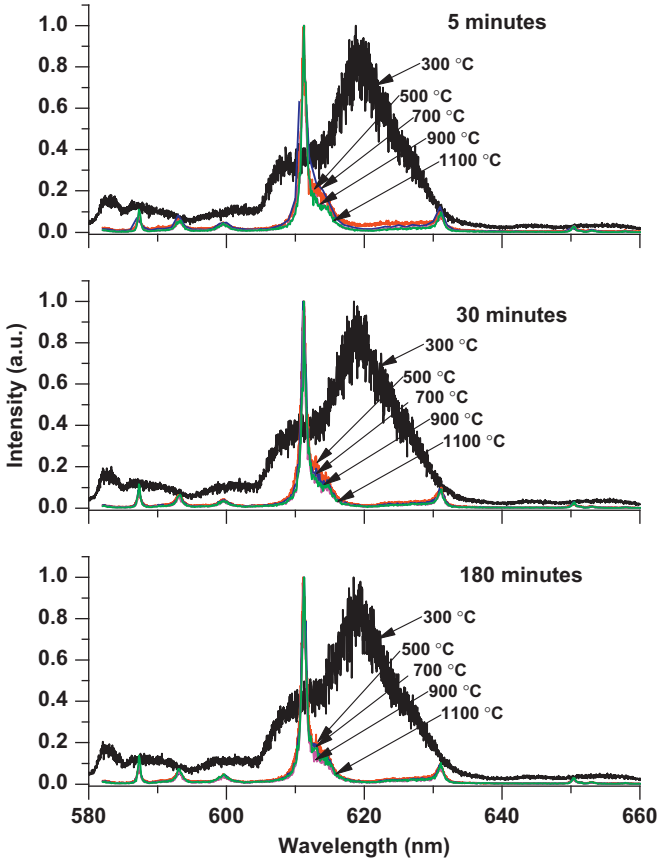

Fig. 10. Normalized fluorescence spectra of Eu-doped yttria precursor calcined at various temperatures for 5 min, 30 min, and 180 min. The spectra were excited at 580.8 nm, except for the 300 °C spectrum, which was excited at 577 nm (excitation at 580.8 nm did not yield any measurable signal).

maximum of about 2.4 ms at 700 °C. Samples heated to higher temperatures show a decrease in fluorescence lifetime. As already seen before, the samples undergo a phase transition at around 665 °C and convert into a crystalline cubic oxide phase. As more and more of the sample material undergoes this transition, the fluorescence lifetime settles at a value of about 1.2 ms, which is typical for cubic Eu:Y_2O_3. At lower temperatures, the fluorescence lifetimes observed are due to the large variety of decomposition products present in the material. The dwell time at each temperature setting does not appear to affect the fluorescence lifetime very much.

The unusual shapes (showing a maximum) of the curves in Fig. 11 can be explained using a concept described by Meltzer et al. [29]. The radiative lifetime of an electronic transition can be described by

$$\tau_R = \frac{1.5 \times 10^4}{f(ED)} \frac{\lambda_0^2}{[(1/3)(n^2+2)]^2 n} \quad (5)$$

where $f(ED)$ is the oscillator strength of the electric dipole transition, λ_0 is the wavelength in vacuum, and n is the index of refraction [30]. Since the size of nanoparticles is much smaller than the wavelength of light, the surroundings of the nanoparticles need to be considered for determining an effective index of refraction. In our experiments, small nanoparticles that already include voids, are heated, and decompose under release of CO_2. As shown in the TEM images in Fig. 6, the decomposition process leads to perforated nanoparticles for samples heated to 500 °C. This perforation leads to an effective decrease of the filling factor for nanoparticles within a certain volume of air. As such, the

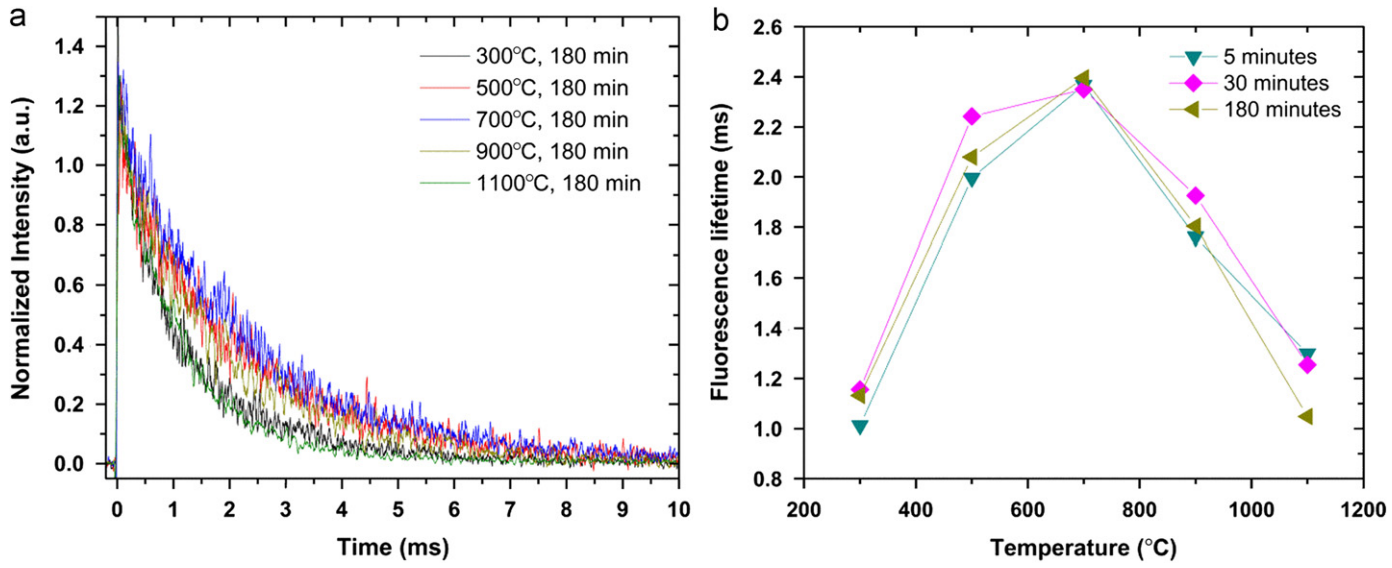

Fig. 11. (a) Traces of fluorescence lifetime and (b) summary of fluorescence lifetime as a function of temperature of Eu-doped yttria precursor, heat treated at various temperatures and dwell times. Samples were excited at 580.8 nm and monitored at 611 nm, except for the sample heated to 300 °C, which was excited at 577 nm and monitored at 620 nm.

effective index of refraction also decreases, leading to an increase of the radiative lifetime according to Eq. (5). For the samples heated to higher temperatures, the grain growth process takes over, increasing the particle size and increasing the effective filling factor.

The FT-IR, XRD, excitation, fluorescence, and fluorescence lifetime data for samples heated to temperatures up to 1100 °C for dwell times between 5 min and 180 min all show that dwell time does not result in any significant differences in the properties of these samples. Different heating temperatures however do result in clearly distinguishable sample properties. This observation indicates that relevant structural changes occur during the initial ramp up and possibly during the first few minutes of the dwell-time.

4. Conclusions

Europium-doped yttrium carbonate nanopowders initially maintained an amorphous phase while undergoing decomposition under heat treatment. During decomposition, the particle size decreases until a crystalline cubic Y_2O_3 phase starts to form. The grain size of this crystalline phase increases with increasing temperature, and most of the grain growth occurs in the early phase of the heating. The grain growth can be fitted to a relaxation equation, providing information about the kinetics of the grain growth process for isothermal heating. Excitation and fluorescence spectra show broad peaks that reflect the presence of the amorphous phases and sharp peaks indicating the crystalline phase. The fluorescence lifetime increases with temperature, reaches a maximum near the temperature where the crystalline phase starts forming, and then decreases to a lower value when only the crystalline phase is present. This lifetime response can be understood by considering the effect of the surrounding medium on the nanoparticles. The effect of the heating temperature is significantly stronger than the effect of dwell time on the optical and structural properties. Most of the changes appear to occur during the ramp up phase or possibly the first few minutes of the dwell time. As such, it can be concluded that the observed changes are mostly due to the effect of temperature and not time. The width of the excitation peak combined with the fluorescence lifetime measurements can be used to track these heat-induced phase transitions and provide information about the heat treatment temperature. Therefore, combining grain growth kinetics and optical data provides a means for ex-situ temperature recording.

Acknowledgment

This work was supported by the Defense Threat Reduction Agency, Basic Research Award # HDTRA1-10-1–0005, and by the Office of Naval Research, Award # N00014-03-1–0247, to Washington State University.

References

[1] E.J. Bosze, G.A. Hirata, J. McKittrick, J. Lumin. 131 (2011) 41–48.
[2] K.L. Choy, J.P. Feist, A.L. Heyes, B. Su, J. Mater. Res. 14 (1999) 3111–3114.
[3] T. Ye, G.W. Zhao, W.P. Zhang, S.D. Xia, Mater. Res. Bull. 32 (1997) 501–506.
[4] K. Marinkovic, L. Mancic, L.S. Gomez, M.E. Rabanal, M. Dramicanin, O. Milosevic, Opt. Mater. 32 (2010) 1606–1611.
[5] A. Pandey, A. Pandey, M.K. Roy, H.C. Verma, Mater. Chem. Phys. 96 (2006) 466–470.
[6] C.N. Wang, Y. Li, W.P. Zhang, M. Yin, Spectrochim. Acta Part a-Mol. Biomol. Spectrosc. 75 (2010) 8–13.
[7] R. Srinivasan, N.R. Yogamalar, J. Elanchezhiyan, R.J. Joseyphus, A.C. Bose, J. Alloys Compd. 496 (2010) 472–477.
[8] H. Huang, G.Q. Xu, W.S. Chin, L.M. Gan, C.H. Chew, Nanotechnology 13 (2002) 318–323.
[9] W.C. Chien, J. Cryst. Growth 290 (2006) 554–559.
[10] Z.G. Huang, X.D. Sun, Z.M. Xiu, S.W. Chen, C.T. Tsai, Mater. Lett. 58 (2004) 2137–2142.
[11] V.K. Pecharsky, P.Y. Zavalij, Fundamentals of Powder Diffraction and Structural Characterization of Materials, Kluwer Academic Publishers, Norwell, 2003.
[12] N. Saito, S. Matsuda, T. Ikegami, J. Am. Ceram. Soc. 81 (1998) 2023–2028.
[13] G. Socrates, Infrared and Raman Characteristic Group Frequencies : Tables and Charts, 3rd ed., Wiley, Chichester, West Sussex, England ; New York, 2001.
[14] W.H. Di, X.G. Ren, L.G. Zhang, C.X. Liu, S.Z. Lu, Crystengcomm 13 (2011) 4831–4833.
[15] Y.J. Zhang, M.R. Gao, K.D. Han, Z.Y. Fang, X.B. Yin, Z.Y. Xu, J. Alloys Compd. 474 (2009) 598–604.
[16] T.S. Chin, R.N. Panda, M.F. Hsieh, R.J. Chung, J. Phys. .Chem. Solids 64 (2003) 193–199.
[17] Y. Sun, L. Qi, M. Lee, B.I. Lee, W.D. Samuels, G.J. Exarhos, J. Lumin. 109 (2004) 85–91.

[18] N. Wang, X. Zhang, Z. Bai, Q. Liu, L. Lu, X. Mi, H. Sun, X. Wang, Powder Technol. 203 (2010) 458–461.
[19] C.A. Traina, J. Schwartz, Langmuir 23 (2007) 9158–9161.
[20] N. Imanaka, T. Masui, Y. Mayama, K. Koyabu, J. Solid State Chem. 178 (2005) 3601–3603.
[21] C.H. Shek, J.K.L. Lai, G.M. Lin, Nanostruct. Mater. 11 (1999) 887–893.
[22] T. Myint, R. Gunawidjaja, H. Eilers, Appl. Phys. Lett. 98 (2011) 171906.
[23] K. Binnemans, Chem. Rev. 109 (2009) 4283–4374.
[24] K. Binnemans, C. Gorllerwalrand, Chem. Phys. Lett. 245 (1995) 75–78.
[25] B. Bihari, H. Eilers, B.M. Tissue, J. Lumin. 75 (1997) 1–10.
[26] B.M. Tissue, H.B. Yuan, J. Solid State Chem. 171 (2003) 12–18.
[27] C. Cascales, C. Zaldo, J. Solid State Chem. 171 (2003) 262–267.
[28] M.L. Debasu, D. Ananias, A.G. Macedo, J. Rocha, L.D. Carlos, J. Phys. Chem. C 115 (2011) 15297–15303.
[29] R.S. Meltzer, S.P. Feofilov, B. Tissue, H.B. Yuan, Phys. Rev. B 60 (1999) 14012–14015.
[30] B. Henderson, G.F. Imbusch, Optical Spectroscopy of Inorganic Solids, Clarendon Press, Oxford, 1989.